RSC Advances

PAPER

View Article Online
View Journal | View Issue

Cite this: *RSC Adv.*, 2017, **7**, 33544

Non-stoichiometric carbon-coated $LiFe_xPO_4$ as cathode materials for high-performance Li-ion batteries†

Ying Feng,[a] Junjie Gu,[b] Feng Yu,[c] Chunfu Lin,[d] Jinli Zhang,[ac] Ning Nie[a] and Wei Li*[a]

A series of non-stoichiometric carbon-coated lithium iron phosphate ($LiFe_xPO_4$/C) have been prepared by a solid-state reaction to study the variation of electrochemical performance at different x values. Characterized by XRD in conjunction with Rietveld refinement, Mössbauer, TEM, Raman, *etc.*, it is indicated that the Li–O bond is elongated in the Fe-poor non-stoichiometric lithium iron phosphate with decreasing x value, while the content of Fe_2P and graphitization degree of carbon layer in $LiFe_xPO_4$/C samples is associated with the ratio of x. The powder electronic conductivity increases from 8.33×10^{-2} S cm^{-1} to 16.67×10^{-2} S cm^{-1} as the x value decreases from 1.04 to 0.98, which is due to a suitable amount of Fe_2P and a superior graphitized carbon layer. Among different Fe/Li ratios, $LiFe_{0.98}PO_4$/C exhibits the highest rate capability of 163.5 mA h g^{-1} at 0.1C and 93.5 mA h g^{-1} at 20C, as well as the largest diffusion coefficient of 12.6×10^{-14} cm^2 s^{-1}. It is illustrated that the synergy effect of elongated Li–O bonds, moderate Fe_2P and graphitized carbon layer results in the high performance of non-stoichiometric $LiFe_xPO_4$/C.

Received 21st April 2017
Accepted 28th June 2017

DOI: 10.1039/c7ra04510g

rsc.li/rsc-advances

1. Introduction

Lithium iron phosphate, with the characteristics of high theoretical capacity, inexpensive cost, environmental benignity and safety,[1–3] except for low electronic conductivity and ionic diffusivity,[4,5] has attracted much attention as a promising cathode material for Li-ion batteries.[6,7] Numerous strategies have been adopted to overcome the intrinsic drawbacks of lithium iron phosphate ($LiFePO_4$), involving surface modification with conductive agents,[8–10] decreasing the particles to nanometer sizes,[11–13] doping with supervalent ions,[14–16] *etc.* In particular, some alien ion dopants have been reported to be capable of tailoring the lattice parameters of $LiFePO_4$ crystals and accelerating the Li-ion migration.[17] Yang *et al.* prepared $LiFe_{0.95}M_{0.05}PO_4$ samples with different doped ions M including Mg^{2+}, Ni^{2+}, Al^{3+}, V^{3+}, respectively, and found that with the dopant of V^{3+} the average Li–O bond length increased from 2.140 Å of undoped $LiFePO_4$ to 2.157 Å of $LiFe_{0.95}V_{0.05}PO_4$, which exhibited larger Li-ion diffusion coefficient and higher discharging capacity of 152 mA h g^{-1} at 0.1C and 136 mA h g^{-1} at 1C.[18] Gao *et al.* investigated the rate capability of Co-doped $LiFe_{1-x}Co_xPO_4$ (x = 0–0.020) and found that $LiFe_{0.99}Co_{0.01}PO_4$ with the largest length of Li–O average bonds exhibited the best electrochemical performance of 114.8 mA h g^{-1} at 10C.[19] Generally, it is considered that the elongation of Li–O bonds can facilitate the Li-ion migration so as to achieve high capacity and decent rate capability.

The Li-ion diffusion channels in the pristine lithium iron phosphate could be blocked by Li–Fe anti-site defects, as reflected by the atomistic modelling[20,21] and experimental characterizations including aberration-corrected high-angle annular dark-field STEM,[22,23] neutron and X-ray diffraction,[24] *etc.*[25,26] To eliminate the negative effect of Li–Fe anti-site defects on the electrochemical performance, the non-stoichiometric lithium iron phosphate have been synthesized recently. For example, Chen *et al.* prepared $Li_{1.08}FePO_4$ by the microwave-assisted hydrothermal method, of which the excess content of Li could inhibit the anti-site defects so as to achieve discharge capacity of 95 mA h g^{-1} at high rate of 10C.[27] Park *et al.* synthesized the lithium-excess $Li_{1.05}Fe_{0.95}PO_4$ by the solid-state reaction, exhibiting 50C rate capability of 78 mA h g^{-1} caused by the elimination of Fe_{Li} defects.[28] On the other hand, there appeared the literature indicating that the non-stoichiometric lithium

[a]*Key Laboratory for Green Chemical Technology MOE, Collaborative Innovation Center of Chemical Science and Chemical Engineering (Tianjin), Key Laboratory of Systems Bioengineering MOE, School of Chemical Engineering & Technology, Tianjin University, Tianjin 300350, People's Republic of China. E-mail: liwei@tju.edu.cn*

[b]*Department of Mechanical and Aerospace Engineering, Carleton University, Ottawa K1S 5B6, Canada*

[c]*Key Laboratory for Green Processing of Chemical Engineering of Xinjiang Bingtuan, School of Chemistry and Chemical Engineering, Shihezi University, Shihezi 832003, People's Republic of China*

[d]*State Key Laboratory of Marine Resource Utilization in South China Sea, College of Materials and Chemical Engineering, Hainan University, Haikou 570228, People's Republic of China*

† Electronic supplementary information (ESI) available: The detailed results of Rietveld refinement, TG measurement and element analysis of $LiFe_xPO_4$/C. See DOI: 10.1039/c7ra04510g

iron phosphate consisted of certain impurities that played a significant role in the electrochemical performance. For instance, Kang and Ceder reported that the fast ion-conducting surface phase of $Li_4P_2O_7$ was responsible for the ultrafast charging and discharging performance of $LiFe_{1-2y}P_{1-y}O_{4-\sigma}$ ($y = 0.05$), which exhibited nearly 100 mA h g^{-1} at 60C.[29] Moreover, Hu *et al.* prepared $LiFe_{1+2x}P_{1+x}O_{4+y}$/C using the solid-state technique, and concluded that the non-stoichiometric sample with 6.5% Fe_2P exhibited better rate performance of 73 mA h g^{-1} at 5C, whereas the stoichiometric sample with 4.5% insulating Li_3PO_4 suffered a rapid decrease of the capacity at 4C.[30] So far no report has been found on the evolution of lattice parameters of the non-stoichiometric lithium iron phosphate crystals, in particular, the variance of Li–O bond length.

In this article, we prepared a series of non-stoichiometric carbon-coated lithium iron phosphate ($LiFe_xPO_4$/C) by a solid-state reaction. For the first time, our work is focused on the fine modulation of Li-ion diffusion channels of non-stoichiometric lithium iron phosphate in view of the variation of crystal lattice parameters. In combination with XRD, Mössbauer, TEM, Raman *etc.*, it is indicated that the elongated Li–O bond appears in the Fe-poor non-stoichiometric lithium iron phosphate. Besides, the content of Fe_2P and the graphitization degree of carbon layer is associated with the ratio of x. Through analysing the Li-ion diffusion coefficient and the electronic conductivity, it is illustrated that the synergy effect of elongated Li–O bonds, moderate Fe_2P and the graphitized carbon layer results in the high performance of non-stoichiometric $LiFe_xPO_4$/C.

2. Experimental

2.1. Material preparation

Non-stoichiometric $LiFe_xPO_4$/C ($x = 0.96, 0.98, 1.02, 1.04$) were synthesized by a solid phase reaction. As a contrast, $LiFe_{1.0}PO_4$/C was prepared in the same way. The starting materials of Li_2CO_3 (99.99%; Shanghai Aladdin Bio-Chem Technology Co., Ltd.), $FeC_2O_4 \cdot 2H_2O$ (99.99%; Alfa Aesar), $NH_4H_2PO_4$ (99.99%; Shanghai Aladdin Bio-Chem Technology Co., Ltd.), and glucose (98%; Shanghai Aladdin Bio-Chem Technology Co., Ltd.) were mixed in a mole ratio of $1 : x : 1 : 0.5$. The glucose was used as a carbon source. In a typical preparation, the reactants were ball-milled in 20 ml of 95 wt% alcohol solution for 6 h then dried under N_2 protection at 25 °C. The pale yellow sample was ground into powder then preheated at 350 °C for 10 h under an N_2 atmosphere. Then the obtained black precursor powder was heated at 700 °C at a heating rate of 5 °C min^{-1}, and held for nearly 6 h to form a crystalline phase $LiFe_xPO_4$/C. Finally, the prepared powder samples were cooled down to ambient temperature and reground before use. The $LiFe_xPO_4$/C samples are denoted in terms of the x value, *e.g.*, $LiFe_{0.96}PO_4$/C is the sample synthesized with the Fe/Li ratio of 0.96. For all the synthesized samples, including $LiFe_{0.96}PO_4$/C, $LiFe_{0.98}PO_4$/C, $LiFe_{1.0}PO_4$/C, $LiFe_{1.02}PO_4$/C, and $LiFe_{1.04}PO_4$/C, the elemental compositions of Li, Fe, P were analysed by Atomic Absorption Spectrometry (AAS), chemical titration, and inductively coupled plasma emission spectrometry (ICP), respectively, as listed in Table S1 in the ESI.† It is indicated that the ratios of Li : Fe : P in all the samples are approximately to the mixing ratio of individual precursor.

2.2. Structural and morphological characterizations

The phase composition were determined by powder XRD (Rigaku D/MAX-2500) in the 2θ range from 10° to 65° with a Cu-Kα radiation ($\lambda = 0.154$ nm) at 40 kV. The scanning step is 4° min^{-1}. The refined structural parameters were calculated by GSAS software, which eliminated the effects of impurities. Room-temperature ^{57}Fe Mössbauer spectra were carried out on a WissEl/MSPCA spectrometer with a ^{57}Co γ-ray radioactive source. The transmitted photons were measured by a proportional counter. The velocity calibration was conducted with the α-Fe spectrum at room temperature.[31] The morphology of the samples and the thickness of carbon layer were observed by JEM-100CX-II high-resolution transmission electron microscopy (HR-TEM) at 100 kV. Thermogravimetry (TG) analysis was obtained on a Netzsch-STA 449C thermal analyser at a heating rate of 10 °C min^{-1} from 25 °C to 700 °C in air to determine the carbon content. Raman spectra were obtained on Renishaw inVia reflex Raman spectrometer equipped with a 532 nm laser. The powder electronic conductivity was detected with four-point probes resistivity measurement system.

2.3. Electrochemical measurements

To test the electrochemical performance, the $LiFe_xPO_4$/C powder was mixed with polyvinylidene fluoride (PVDF) and battery grade acetylene black (80 : 10 : 10 wt%) in *N*-methylpyrrolidinone under magnetic stirring for 10 h. Next, the viscous black slurry was spread onto aluminum foil then dried for 12 h at 80 °C. The cathode films were punched into 1.3 cm diameter discs after roll-pressing, and dried at 120 °C in vacuum overnight. The electrolyte was prepared by dissolving 1 M $LiPF_6$ in the mixed solvent of ethylene carbonate (EC) and dimethyl carbonate (DMC). We assembled Li/$LiFe_xPO_4$ cells with standard CR2032 coin cell hardware fittings in an argon-filled glove box with H_2O and O_2 content under 0.1 ppm. The pieces of $LiFe_xPO_4$/C cathode were separated by Celgard 2400 from lithium metal anodes. Charge/discharge cycle performance tests were conducted on a LAND-CT2011A battery test system (Wuhan, China) in voltages of 2.0 to 4.2 V at different rates. The electrochemical impedance spectroscopic analysis (EIS) was performed on a CHI660E electrochemical analyser (CH Instruments, China) with a 0.005 V amplitude signal with the frequency range from 0.1 Hz to 100 kHz, and the data was fitted by Z-view software. The cycle voltammetry (CV) test was performed on the electrochemical analyser (CH1604A, CH Instruments, China) at the scan rate of 0.1 mV s^{-1}.

3. Results and discussion

3.1. Structural characterization

The XRD patterns (Fig. 1) present the composition of $LiFe_xPO_4$/C. For $LiFe_xPO_4$/C with the x value unequal to 1.0, the major peaks are located similarly to the standard orthorhombic

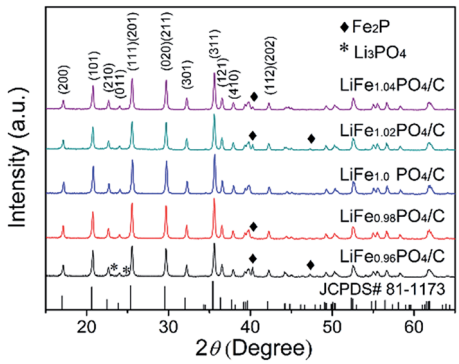

Fig. 1 XRD patterns of $LiFe_xPO_4/C$.

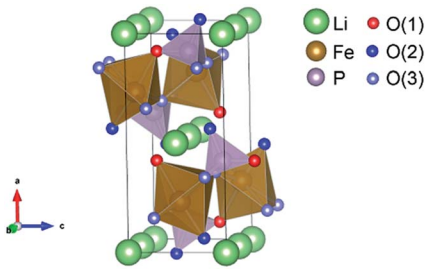

Fig. 2 Illustration of the atomic structure of $LiFePO_4$.

structure of $LiFe_{1.0}PO_4/C$ confirmed with ICPDS file (no. 81-1173) except for small peaks of some impurities. In the case of $LiFe_{0.96}PO_4/C$, there are peaks of the impurities of Li_3PO_4 and Fe_2P, while other non-stoichiometric samples including $LiFe_{0.98}PO_4/C$, $LiFe_{1.02}PO_4/C$ and $LiFe_{1.04}PO_4/C$ there exist the peaks of Fe_2P impurity. Table 1 lists the refined lattice parameters, cell volume V, crystal size of particles, and carbon content of $LiFe_xPO_4/C$ composites. The crystal size of particles were calculated according to the (311) diffraction peak in Fig. 1 by Scherrer's equation (*i.e.*, $D_{(311)} = 0.9\lambda/\beta \cos\theta$).[32] The average crystalline size is respectively 64.5, 68, 71, 72.3, and 75.1 nm for $LiFe_{0.96}PO_4/C$, $LiFe_{0.98}PO_4/C$, $LiFe_{1.0}PO_4/C$, $LiFe_{1.02}PO_4/C$, and $LiFe_{1.04}PO_4/C$, suggesting that the crystalline size decreases at lower Fe/Li ratio.

To demonstrate the variation in the local structure of $LiFe_xPO_4/C$, the bond length parameters were calculated from Rietveld refinement using powder XRD data at room temperature. Fig. S1 and Table S2† present the detailed results of Rietveld refinement. To make the discussion clear, the oxygen atoms are classified into several groups according to previous literature.[33] We focused on the interatomic distances around Fe and Li, displayed in Fig. 2. Table 2 lists the refined bond length parameters of $LiFe_xPO_4/C$. The Li–O(1) bond length of $LiFe_{1.0}PO_4/C$ is 2.161 Å, whereas it increases to 2.176 Å and 2.184 Å as the x value decreases to 0.98 and 0.96. Similarly, the values of Li–O(2) and Li–O(3) bond lengths rise at x values lower than 1.0. On the other hand, the bond lengths of Fe–O(1), Fe–O(2) and Fe–O(3) decrease with decreasing x values. Combining the results of Tables 1 and 2, it is demonstrated that $LiFe_{0.96}PO_4/C$ and $LiFe_{0.98}PO_4/C$ possess the enlarged Li–O bond length as well as the shorter diffusion distance in crystal particles in contrast to $LiFe_{1.0}PO_4/C$, which would be promising to achieve enhanced rate capability with improved rate of Li-ion extraction/intercalation.

Table 1 Refined lattice parameters, cell volume V and crystal size $D_{(311)}$ of $LiFe_xPO_4/C$

Sample	a (Å)	b (Å)	c (Å)	V (Å^3)	$D_{(311)}$ (nm)
$LiFe_{0.96}PO_4/C$	10.3392	6.0150	4.7004	292.323	64.5
$LiFe_{0.98}PO_4/C$	10.3393	6.0154	4.7004	292.347	68
$LiFe_{1.0}PO_4/C$	10.3368	6.0141	4.7006	292.222	71
$LiFe_{1.02}PO_4/C$	10.3365	6.0142	4.7006	292.213	72.3
$LiFe_{1.04}PO_4/C$	10.3372	6.0141	4.7005	292.225	75.1

3.2. Mössbauer spectra

In order to determine the amount of impurity phases, the ^{57}Fe Mössbauer spectra were carried out at room temperature. As shown in Fig. 3, all spectra curves contain two doublets which means two different iron environments in $LiFe_xPO_4/C$. The green curves correspond to octahedral Fe^{2+} in $LiFePO_4$, while the blue curves are due to the presence of Fe_2P. For Fe^{2+} in $LiFePO_4$, the isomer shift (IS) of the green symmetrical doublet is 1.23 mm s^{-1}, and the quadrupole splitting (QS) is 2.99 mm s^{-1}. Compared to the IS and QS values in previous literature, the parameters of the blue doublet are similar to that of Fe^{3+} at 3*f* site in Fe_2P,[34,35] which is formed due to the following carbon-thermal reduction:

$$6LiFePO_4 + 8C \rightarrow 3Fe_2P + 2Li_3PO_4 + P\uparrow + 8CO_2\uparrow \quad (1)$$

Table 3 lists the Mössbauer parameters and the percentage of iron in different environments. When every mole of Fe_2P is generated, there appears 2/3 mole of Li_3PO_4 according to eqn (1). In order to obtain the accurate content of Fe_2P, the fraction of Li_3PO_4 should be taken into account. The weight and mole percent of Fe_2P, Li_3PO_4 and $LiFePO_4$ in $LiFe_xPO_4/C$ samples are listed in Table 4. The calculated weight ratio of Fe_2P is 12.82 wt% for $LiFe_{0.96}PO_4/C$, 5.34 wt% for $LiFe_{0.98}PO_4/C$, 4.95 wt% for $LiFe_{1.0}PO_4/C$, 8.36 wt% for $LiFe_{1.02}PO_4/C$ and 9.32 wt% for $LiFe_{1.04}PO_4/C$. Because ^{57}Fe Mössbauer spectra are highly sensitive to detect both crystalline and non-crystalline phases, the results indicate the existence of small amount of Fe_2P impurity in $LiFe_{1.0}PO_4/C$, although the peak is not detectable in XRD pattern. Previously, Fe_2P was reported to have an amphoteric effect on the electrochemical properties of $LiFePO_4$, suggesting that Fe_2P can only serve an electronic conductive function when its concentration is maintained below a critical value.[36] Compared to $LiFe_{1.0}PO_4/C$, the excessive Fe_2P in $LiFe_{1.02}PO_4/C$ and $LiFe_{1.04}PO_4/C$ would probably block the one-dimensional diffusion channel and reduce the Li-ion mobility, leading to the degradation of the rate capability and cycle performance, which can be deduced in $LiFe_{0.96}PO_4/C$ in the same way.

Table 2 Refined bond length parameters of $LiFe_xPO_4/C$

	Interatomic distance (Å)					
Samples	Fe–O(1)	Fe–O(2)	Fe–O(3)	Li–O(1)	Li–O(2)	Li–O(3)
$LiFe_{0.96}PO_4/C$	2.216(8)	2.052(10)	2.265(5)	2.184(6)	2.120(5)	2.153(6)
$LiFe_{0.98}PO_4/C$	2.209(7)	2.066(8)	2.271(4)	2.176(5)	2.102(4)	2.139(5)
$LiFe_{1.0}PO_4/C$	2.219(7)	2.067(8)	2.275(4)	2.161(4)	2.100(4)	2.135(5)
$LiFe_{1.02}PO_4/C$	2.215(7)	2.064(8)	2.268(4)	2.165(5)	2.099(4)	2.132(5)
$LiFe_{1.04}PO_4/C$	2.216(8)	2.057(9)	2.271(5)	2.160(5)	2.102(5)	2.129(6)

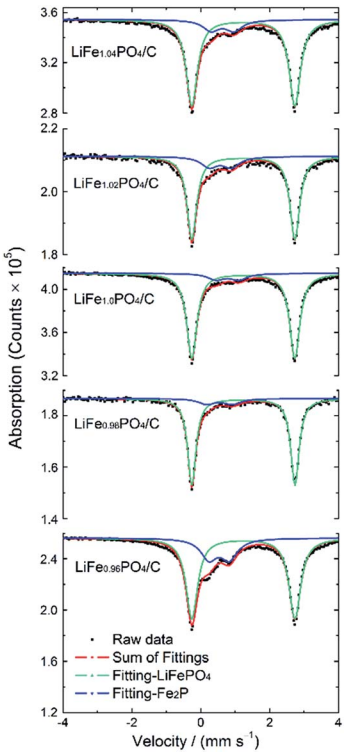

Fig. 3 Mössbauer spectra of $LiFe_xPO_4/C$.

3.3. Morphological characterization

Fig. 4 displays the HR-TEM images of the $LiFe_xPO_4/C$ samples. It is indicated that all of the samples consist of similar spherical particles with the particle size distribution around 30–100 nm (Fig. 4(a)–(e)). Some flocculent carbon structure appear between particles, which provide a larger contact area on the particle–particle and electrode–electrolyte interface, alleviating the diffusion limitation problems. The thickness of the amorphous carbon coating layer varies between 5–10 nm (Fig. 4(f)–(j)), contributing to improve the electronic conductivity. The carbon content measured by TG analysis are 13.21 wt%, 14.59 wt%, 14.18 wt%, 12.99 wt% and 12.77 wt% for $LiFe_{0.96}PO_4/C$, $LiFe_{0.98}PO_4/C$, $LiFe_{1.0}PO_4/C$, $LiFe_{1.02}PO_4/C$, and $LiFe_{1.04}PO_4/C$, respectively (Table S3 and Fig. S2†).

3.4. Raman spectra

Aiming to clarify the conductivity contribution of the carbon layer, Raman spectra were adopted to investigate the degree of carbon disorder on the surface of $LiFe_xPO_4/C$. As Fig. 5 shows, the two dominant peaks around 1350 cm^{-1} and 1580 cm^{-1} represent disorder (D) band and graphitic (G) band, respectively.[37] The D band is characteristic of the disordered structure ascribed to the breathing vibration at the boundary of graphene sheet, whereas the G band is corresponding to bond stretching of the graphitized carbon atoms.[38] Graphitized carbon is known to possess better electronic conductivity than disordered carbon. Generally, the peak intensity ratio (I_D/I_G) is used to

Table 4 The weight and mole percent of Fe_2P, Li_3PO_4 and $LiFePO_4$ in $LiFe_xPO_4/C$

	Fe_2P		Li_3PO_4		$LiFePO_4$	
Samples	wt%	mol%	wt%	mol%	wt%	mol%
$LiFe_{0.96}PO_4/C$	12.82	13.60	6.94	9.09	80.24	77.31
$LiFe_{0.98}PO_4/C$	5.34	5.84	2.89	3.87	91.77	90.29
$LiFe_{1.0}PO_4/C$	4.95	5.39	2.68	3.59	92.37	91.02
$LiFe_{1.02}PO_4/C$	8.36	9.01	4.52	6.01	87.12	84.98
$LiFe_{1.04}PO_4/C$	9.32	10.02	5.04	6.68	85.64	83.30

Table 3 ^{57}Fe Mössbauer spectra and fitted data for $LiFe_xPO_4/C$

	Fe^{3+} in Fe_2P				Fe^{2+} in $LiFePO_4$			
Samples	IS (mm s^{-1})	QS (mm s^{-1})	Γ (FWHM)	mol%	IS (mm s^{-1})	QS (mm s^{-1})	Γ (FWHM)	mol%
$LiFe_{0.96}PO_4/C$	0.5345	0.5927	0.582	26.1	1.2377	2.9951	0.408	73.9
$LiFe_{0.98}PO_4/C$	0.5474	0.7505	0.582	11.4	1.2369	2.9954	0.292	88.6
$LiFe_{1.0}PO_4/C$	0.7761	0.6655	0.582	10.6	1.2367	2.9914	0.355	89.4
$LiFe_{1.02}PO_4/C$	0.5682	0.6364	0.582	17.5	1.2370	2.9937	0.338	82.5
$LiFe_{1.04}PO_4/C$	0.6338	0.6660	0.582	19.4	1.2371	2.9936	0.394	80.6

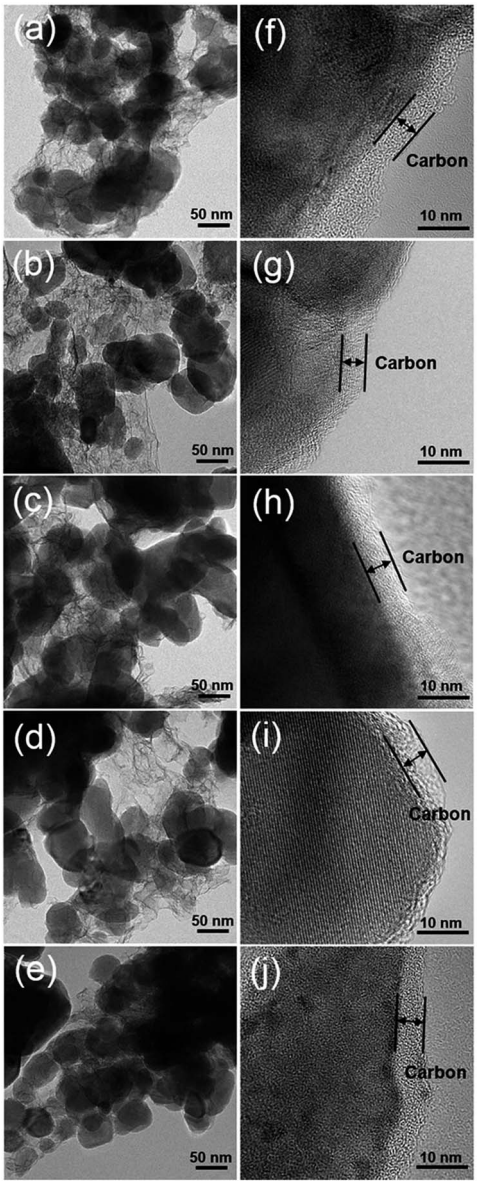

Fig. 4 TEM images of $LiFe_{0.96}PO_4/C$ (a) and (f), $LiFe_{0.98}PO_4/C$ (b) and (g), $LiFe_{1.0}PO_4/C$ (c) and (h), $LiFe_{1.02}PO_4/C$ (d) and (i), and $LiFe_{1.04}PO_4/C$ (e) and (j).

indicate the graphitization of the carbon layers. As listed in Table 5, the $LiFe_{0.98}PO_4/C$ shows relatively higher degree of graphitization than the others.

3.5. Electrochemical characterizations

Fig. 6 shows the electrochemical performances of $LiFe_xPO_4/C$ samples. Fig. 6(a) presents the profiles of initial charge/discharge capacity *versus* potential from 2.2 V to 4.2 V at 0.1C. The flat voltage plateaus from 3.39 V to 3.46 V correspond to the redox reaction between $LiFePO_4$ and $FePO_4$.[39,40] From the result of Fig. 6(a), the discharge capacities of $LiFe_{0.96}PO_4/C$, $LiFe_{0.98}PO_4/C$, $LiFe_{1.0}PO_4/C$, $LiFe_{1.02}PO_4/C$, and $LiFe_{1.04}PO_4/C$ are 157.7 mA h g^{-1}, 163.5 mA h g^{-1}, 153.7 mA h g^{-1}, 148 mA h g^{-1}, and 143.5 mA h g^{-1}, respectively. The corresponding coulombic

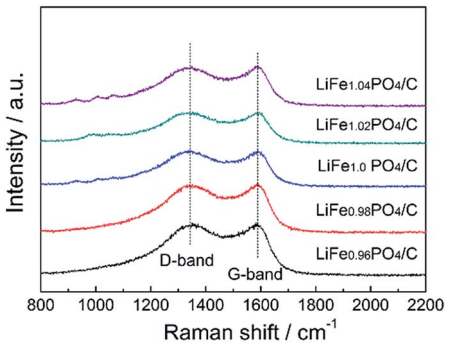

Fig. 5 Raman spectra of $LiFe_xPO_4/C$.

Table 5 I_D/I_G values of $LiFe_xPO_4/C$

Samples	I_D/I_G
$LiFe_{0.96}PO_4/C$	0.993
$LiFe_{0.98}PO_4/C$	0.986
$LiFe_{1.0}PO_4/C$	0.998
$LiFe_{1.02}PO_4/C$	0.994
$LiFe_{1.04}PO_4/C$	1.001

efficiencies are calculated as 95.9%, 96.3%, 94.3%, 94.3% and 95%. Furthermore, the rate capability of $LiFe_xPO_4/C$ are illustrated with five cycles at every rates of 0.1C, 1C, 2C, 5C, 10C and 20C in Fig. 6(b), indicating the superior performance of $LiFe_{0.98}PO_4/C$. The loading amount of the active material in the each cathode are 1.07, 1.07, 1.02, 1.06 and 1.08 mg cm^{-2} for $LiFe_{0.96}PO_4/C$, $LiFe_{0.98}PO_4/C$, $LiFe_{1.0}PO_4/C$, $LiFe_{1.02}PO_4/C$, and $LiFe_{1.04}PO_4/C$, respectively. As Fig. 6(c) shows, all of the $LiFe_xPO_4/C$ samples demonstrate excellent cycle performance at 20C. The capacity retention rates after 100 cycles are 98.8%, 99.2%, 98.7%, 97.4% and 90.2%, respectively. In particular, $LiFe_{0.98}PO_4/C$ retains 90.9% capacity even after 500 cycles, as shown in Fig. 6(d). It is illustrated that Fe-poor $LiFe_{0.98}PO_4/C$ exhibits the outstanding discharge capacity, coulombic efficiency and rate capability, which could be attributed to the faster Li-ion migration and enhanced electronic conductivity originated from the elongated Li–O bond lengths, appropriate content of Fe_2P and highly graphitized carbon layer on the grain surface. Although $LiFe_{0.96}PO_4/C$ has the longest Li–O bond length (Table 2), too much content of Fe_2P blocks the Li-ion diffusion pathways and hinders Li-ion movement, resulting in an inferior discharge capacity of $LiFe_{0.96}PO_4/C$ comparing with $LiFe_{0.98}PO_4/C$.

The first-around CVs profiles of $LiFe_xPO_4/C$ are shown in Fig. 7(a). It can be seen that all the CV curves consist of distinct anodic peaks and cathode peaks, corresponding to the extraction and insertion process of Li ions, respectively. Among them, $LiFe_{0.98}PO_4/C$ shows the sharpest redox peaks, implying the superior electrode kinetics. According to the CV curves, it is indicated that the peak potential difference between anodic and cathode peak is 0.145 V for $LiFe_{0.98}PO_4/C$, 0.171 V for $LiFe_{0.96}PO_4/C$, 0.187 V for $LiFe_{1.0}PO_4/C$, 0.201 V for $LiFe_{1.02}PO_4/C$, 0.263 V for $LiFe_{1.04}PO_4/C$, respectively. Thus, $LiFe_{0.98}PO_4/C$ exhibits the smallest value of the potential interval and the

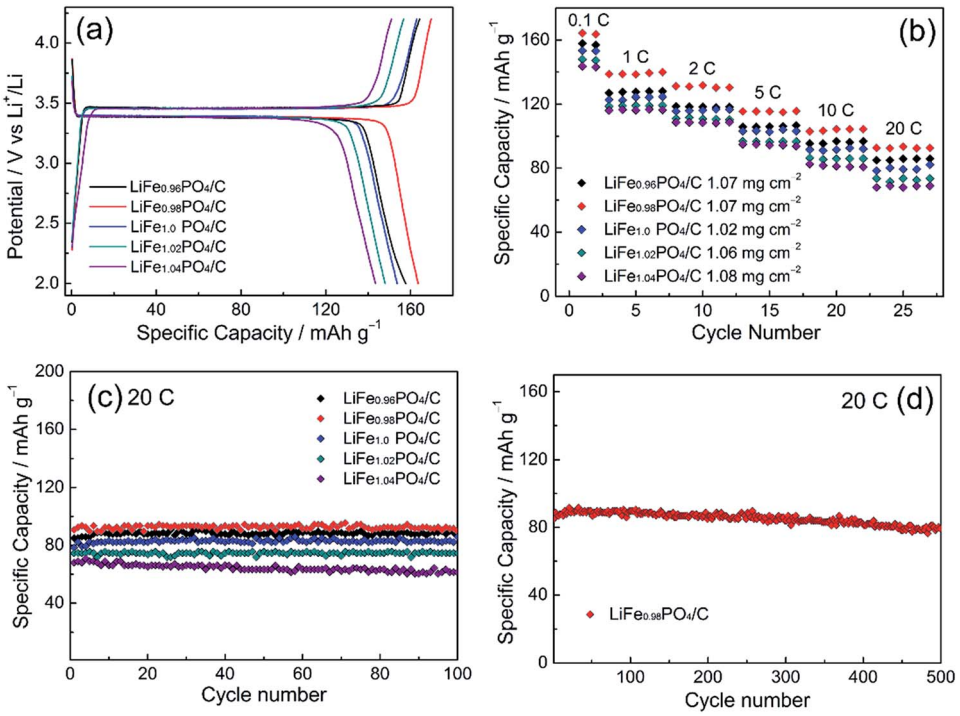

Fig. 6 Electrochemical performance of $LiFe_xPO_4/C$: (a) initial charge/discharge curves at 0.1C; (b) the multi-rate capability and cycle performance; (c) performance within 100 cycles at 20C and (d) 500-cycle performance for $LiFe_{0.98}PO_4/C$ at 20C.

highest peak current in CV curves, suggesting an enhanced electrode reaction reversibility and a better rate capability, which is consistent with the electrochemical performance shown in Fig. 6.

The electrode reaction dynamics and Li-ion diffusion characteristics of $LiFe_xPO_4/C$ were studied by electrochemical impedance spectroscopy (EIS). Fig. 7(b) displays the concise equivalent circuit model applied to analyse the impedance

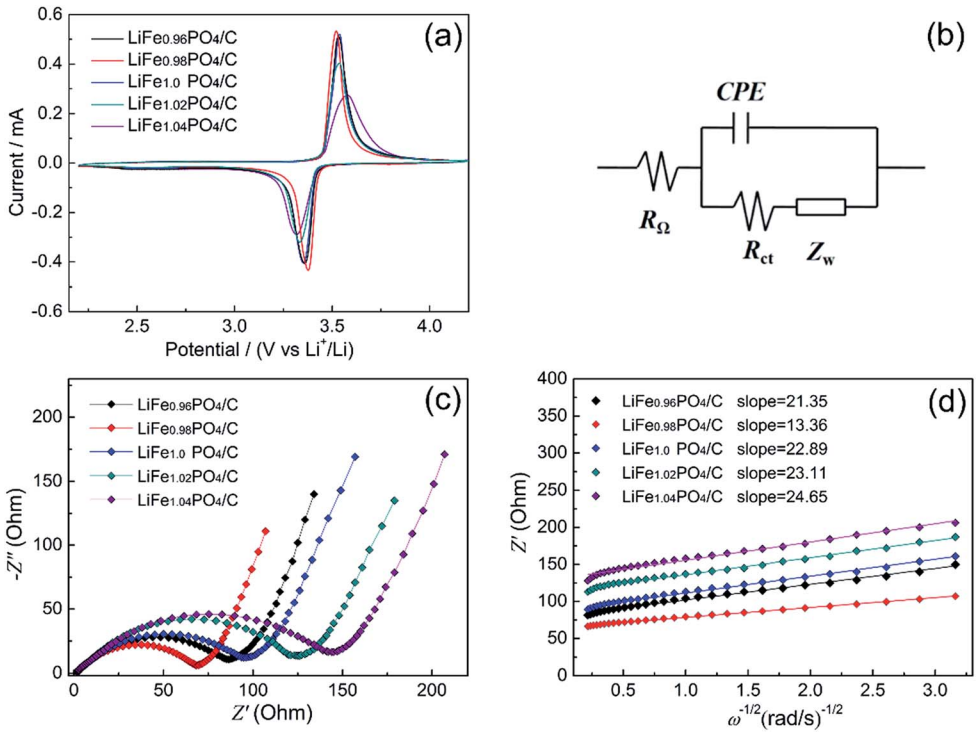

Fig. 7 (a) Cyclic voltammograms of the $LiFe_xPO_4/C$ at the scan rate of 0.1 mV s^{-1}; (b) equivalent circuit model; (c) Nyquist plots of the $LiFe_xPO_4/C$ samples; (d) the relationship between Z' and the reciprocal square root of the angular frequency ($\omega^{-1/2}$).

Table 6 The fitting results of the data given in Fig. 7 using sectionalized simulation and the powder electronic conductivity of $LiFe_xPO_4/C$ detected by four-point probe method

Sample	R_Ω (Ω cm^2)	R_{ct} (Ω)	D_{Li^+} ($\times 10^{-14}$ cm^2 s^{-1})	Electronic conductivity (10^{-2} S cm^{-1})
$LiFe_{0.96}PO_4/C$	1.077	88.85	8.48	7.69
$LiFe_{0.98}PO_4/C$	1.866	68.78	12.6	16.67
$LiFe_{1.0}PO_4/C$	1.582	101.6	7.38	14.29
$LiFe_{1.02}PO_4/C$	1.700	130.2	7.24	9.09
$LiFe_{1.04}PO_4/C$	1.209	152.3	6.36	8.33

spectra which is shown in Fig. 7(c). Here, R_Ω refers to the ohmic resistance of electrolyte presented as intercept on the abscissa axis at high frequency. The component CPE (constant phase angle element) reflects the impedance caused by irregular surface structure and energy barrier at mass and charge transfer.[41] The R_{ct} component represents the charge transfer resistance appearing in electrochemical reactions, which includes the resistances derived from particle–particle and electrolyte–electrode contacts, and exhibits as a semicircle within the medium frequency region. The Warburg impedance Z_W is associated with the diffusion kinetics of Li ions in the crystal lattice, corresponding to the inclined line in the low frequency. Furthermore, the Li-ion diffusion coefficient D for each sample can be computed as follows:[42]

$$D = R^2T^2/2A^2n^4F^4C^2\sigma^2 \quad (2)$$

where R refers to the gas constant (8.314 J mol^{-1} K^{-1}), T is the absolute temperature (298 K), A is the surface area of the cathode, n represents the number of electrons per molecule during oxidation, F is the Faraday constant (96 485.333C mol^{-1}), C is the concentration of Li ions, and σ represents the Warburg factor connected with Z':

$$Z' = R_D + R_L + \sigma\omega^{-1/2} \quad (3)$$

where R_D and R_L are the resistance of charge transfer and solution resistance, respectively, and σ is the angular frequency ($2\pi f$). Fig. 7(d) reflects the relationship between Z' and $\omega^{-1/2}$ in the low-frequency region. The slopes of the individual lines are the outcome of linear least squares fitting, and the scattered points represent the experimental values. The values of D for Li ions in the samples are calculated according to the slope parameters in Fig. 7(d) and eqn (2) and (3). In addition, the powder electronic conductivity were detected by four-point probe methods. Both the simulated and calculated parameters and the value of electronic conductivity of $LiFe_xPO_4/C$ samples are listed in Table 6.

Obviously, R_{ct} decreases according to the Fe/Li ratio in descending order, except for $LiFe_{0.98}PO_4/C$, which shows the lowest charge transfer resistance of 68.78 Ω and the highest electronic conductivity of 16.67 $\times$ 10^{-2} S cm^{-1}. It can be ascribed to the moderate Fe_2P and superior graphitization degree of carbon layer. In addition, it was reported that the increase of active sites was represented by a decreasing semicircle diameter and increasing frequency at which the sloping line begins.[43] Here, the EIS data suggest the reason for the better cycle stability and electrochemical performance observed for the $LiFe_{0.98}PO_4/C$ sample, which exhibits the smallest semicircle diameter. The exchange current density i_o is obtained from R_{ct} using eqn (4):

$$i_o = RT/nFR_{ct} \quad (4)$$

where n is the charge transfer number per molecule during intercalation. The value of i_o obtained for the $LiFe_{0.98}PO_4/C$ sample is 0.37 mA, which is higher than 0.29 mA for $LiFe_{0.96}PO_4/C$, 0.25 mA for $LiFe_{1.0}PO_4/C$, 0.19 mA for $LiFe_{1.02}PO_4/C$ and 0.17 mA for $LiFe_{1.04}PO_4/C$.

In general, the value of exchange current density is associated with the reversibility of electrode.[44] $LiFe_{0.98}PO_4/C$ exhibits the higher current density than any of others, which coincides with the optimal battery performance. As shown in Table 6, the value of D for Li ions in the $LiFe_{0.98}PO_4/C$ sample is calculated as 12.6 $\times$ 10^{-14} cm^2 s^{-1}, which is considerably greater than the values of other samples, which is 8.48 $\times$ 10^{-14}, 7.38 $\times$ 10^{-14}, 7.24 $\times$ 10^{-14} and 6.36 $\times$ 10^{-14} cm^2 s^{-1} for $LiFe_{0.96}PO_4/C$, $LiFe_{1.0}PO_4/C$ $LiFe_{1.02}PO_4/C$ and $LiFe_{1.04}PO_4/C$, respectively. Thus, it is reasonable to conclude that the enlarged Li–O bond lengths in non-stoichiometric Fe-poor $LiFe_{0.98}PO_4/C$ result in the accelerated Li-ion migration through the $LiFePO_4$ bulk and electrode–electrolyte interface *via* enhanced Li-ion intercalation/de-intercalation processes, consequently achieving the high electrochemical performance.

4. Conclusions

Non-stoichiometric $LiFe_xPO_4/C$ (x = 0.96, 0.98, 1.02, 1.04) cathode materials have been synthesized by a simple solid-state reaction. Based on the refined lattice parameters, it is indicated that the Fe-poor samples possess the enlarged Li–O bond lengths, facilitating the Li-ion migration. Moreover, Mössbauer spectra show that the content of Fe_2P impurity is related to Fe/Li ratio, which enhances the conductivity at low concentration. The graphitization degree of carbon is slightly elevated with high content of carbon. Due to the enlarged Li–O bond length, proper content of Fe_2P impurity and relatively high graphitization degree of carbon layer, the Li-ion diffusivity and electronic conductivity of $LiFe_{0.98}PO_4/C$ are superior to other non-stoichiometric samples. The synergy effect of these factors makes $LiFe_{0.98}PO_4/C$ exhibit the highest discharge capacity, rate capability, as well as excellent cycle performance. The disclosed

relationship among the crystal lattice parameters, the composition and the electrochemical performance of non-stoichiometric $LiFe_xPO_4/C$ provides a pathway to design new material of other type olivine phosphate so as to improve the electrochemical performance.

Acknowledgements

This work was financially supported by the National Natural Science Foundation of China (No. 21476158, 21621004), and Program for Changjiang Scholars and Innovative Research Team in University (No. IRT_15R46).

Notes and references

1 A. Padhi, K. Nanjundaswamy, C. Masquelier, S. Okada and J. Goodenough, *J. Electrochem. Soc.*, 1997, **144**, 1609–1613.
2 L.-X. Yuan, Z.-H. Wang, W.-X. Zhang, X.-L. Hu, J.-T. Chen, Y.-H. Huang and J. B. Goodenough, *Energy Environ. Sci.*, 2011, **4**, 269–284.
3 G. Pagot, F. Bertasi, G. Nawn, E. Negro, G. Carraro, D. Barreca, C. Maccato, S. Polizzi and V. Di Noto, *Adv. Funct. Mater.*, 2015, **25**, 4032–4037.
4 F. Yu, L. Zhang, Y. Li, Y. An, M. Zhu and B. Dai, *RSC Adv.*, 2014, **4**, 54576–54602.
5 Z. Yang, Y. Dai, S. Wang and J. Yu, *J. Mater. Chem. A*, 2016, **4**, 18210–18222.
6 M. M. Thackeray, C. Wolverton and E. D. Isaacs, *Energy Environ. Sci.*, 2012, **5**, 7854–7863.
7 J. B. Goodenough and K. S. Park, *J. Am. Chem. Soc.*, 2013, **135**, 1167–1176.
8 J. Zhang, N. Nie, Y. Liu, J. Wang, F. Yu, J. Gu and W. Li, *ACS Appl. Mater. Interfaces*, 2015, **7**, 20134–20143.
9 Z. Jinli, W. Jiao, L. Yuanyuan, N. Ning, G. Junjie, Y. Feng and L. Wei, *J. Mater. Chem. A*, 2015, **3**, 2043–2049.
10 Y. Liu, J. Gu, J. Zhang, F. Yu, J. Wang, N. Nie and W. Li, *RSC Adv.*, 2015, **5**, 9745–9751.
11 Y. Liu, J. Gu, J. Zhang, J. Wang, N. Nie, Y. Fu, W. Li and F. Yu, *Electrochim. Acta*, 2015, **173**, 448–457.
12 D. Rangappa, K. Sone, T. Kudo and I. Honma, *J. Power Sources*, 2010, **195**, 6167–6171.
13 J. Lee and A. S. Teja, *Mater. Lett.*, 2006, **60**, 2105–2109.
14 A. Moretti, G. Giuli, F. Nobili, A. Trapananti, G. Aquilanti, R. Tossici and R. Marassi, *J. Electrochem. Soc.*, 2013, **160**, A940–A949.
15 D. Jang, K. Palanisamy, J. Yoon, Y. Kim and W.-S. Yoon, *J. Power Sources*, 2013, **244**, 581–585.
16 S. Novikova, S. Yaroslavtsev, V. Rusakov, A. Chekannikov, T. Kulova, A. Skundin and A. Yaroslavtsev, *J. Power Sources*, 2015, **300**, 444–452.
17 R. Qing, M.-C. Yang, Y. S. Meng and W. Sigmund, *Electrochim. Acta*, 2013, **108**, 827–832.
18 M.-R. Yang and W.-H. Ke, *J. Electrochem. Soc.*, 2008, **155**, A729–A732.
19 H. Gao, L. Jiao, J. Yang, Z. Qi, Y. Wang and H. Yuan, *Electrochim. Acta*, 2013, **97**, 143–149.
20 C. A. J. Fisher, V. M. H. Prieto and M. S. Islam, *Chem. Mater.*, 2008, **20**, 5907–5915.
21 M. S. Islam, D. J. Driscoll, C. A. J. Fisher and P. R. Slater, *Chem. Mater.*, 2005, **17**, 5085–5092.
22 S. Y. Chung, S. Y. Choi, T. Yamamoto and Y. Ikuhara, *Phys. Rev. Lett.*, 2008, **100**, 125502.
23 S.-Y. Chung, Y.-M. Kim and S.-Y. Choi, *Adv. Funct. Mater.*, 2010, **20**, 4219–4232.
24 S.-P. Badi, M. Wagemaker, B. L. Ellis, D. P. Singh, W. J. H. Borghols, W. H. Kan, D. H. Ryan, F. M. Mulder and L. F. Nazar, *J. Mater. Chem.*, 2011, **21**, 10085.
25 S. Yang, Y. Song, P. Y. Zavalij and M. S. Whittingham, *Electrochem. Commun.*, 2002, **4**, 239–244.
26 P. Axmann, C. Stinner, M. Wohlfahrt-Mehrens, A. Mauger, F. Gendron and C. M. Julien, *Chem. Mater.*, 2009, **21**, 1636–1644.
27 R. Chen, X. Wang and X. Kong, *Mater. Lett.*, 2014, **120**, 76–78.
28 K. Y. Park, I. Park, H. Kim, G. Yoon, H. Gwon, Y. Cho, Y. S. Yun, J. J. Kim, S. Lee and D. Ahn, *Energy Environ. Sci.*, 2016, **9**, 2902–2915.
29 B. Kang and G. Ceder, *Nature*, 2009, **458**, 190–193.
30 C. Hu, H. Yi, H. Fang, B. Yang, Y. Yao, W. Ma and Y. Dai, *Mater. Lett.*, 2011, **65**, 1323–1326.
31 X. Li, L. Yuan, J. Wang, L. Jiang, A. I. Rykov, D. L. Nagy, C. Bogdan, M. A. Ahmed, K. Zhu, G. Sun and W. Yang, *Nanoscale*, 2016, **8**, 2333–2342.
32 H. Shang, W. Chu, J. Cheng, F. Pan, D. Cheng, D. Xia, W. Wang and Z. Wu, *J. Mater. Chem. A*, 2013, **1**, 6635–6641.
33 N. Meethong, Y.-H. Kao, S. A. Speakman and Y.-M. Chiang, *Adv. Funct. Mater.*, 2009, **19**, 1060–1070.
34 K. S. Dhindsa, A. Kumar, G. A. Nazri, V. M. Naik, V. K. Garg, A. C. Oliveira, P. P. Vaishnava, Z. X. Zhou and R. Naik, *J. Solid State Electrochem.*, 2016, **20**, 2275–2282.
35 Y.-H. Rho, L. F. Nazar, L. Perry and D. Ryan, *J. Electrochem. Soc.*, 2007, **154**, A283–A289.
36 M.-S. Song, D.-Y. Kim, Y.-M. Kang, Y.-I. Kim, J.-Y. Lee and H.-S. Kwon, *J. Power Sources*, 2008, **180**, 546–552.
37 J. Zhu, K. Yoo, I. El-Halees and D. Kisailus, *ACS Appl. Mater. Interfaces*, 2014, **6**, 21550–21557.
38 K. F. Hsu, S. Y. Tsay and B. J. Hwang, *J. Mater. Chem.*, 2004, **14**, 2690–2695.
39 B. Wang, Y. Qiu and L. Yang, *Electrochem. Commun.*, 2006, **8**, 1801–1805.
40 Y. Xia, W. Zhang, H. Huang, Y. Gan, J. Tian and X. Tao, *J. Power Sources*, 2011, **196**, 5651–5658.
41 M. Lebrini, M. Lagrenée, H. Vezin, M. Traisnel and F. Bentiss, *Corros. Sci.*, 2007, **49**, 2254–2269.
42 H. Liu, C. Li, H. P. Zhang, L. J. Fu, Y. P. Wu and H. Q. Wu, *J. Power Sources*, 2006, **159**, 717–720.
43 J. Molenda, W. Ojczyk and J. Marzec, *J. Power Sources*, 2007, **174**, 689–694.
44 H. Shu, X. Wang, W. Wen, Q. Liang, X. Yang, Q. Wei, B. Hu, L. Liu, X. Liu, Y. Song, M. Zho, Y. Bai, L. Jiang, M. Chen, S. Yang, J. Tan, Y. Liao and H. Jiang, *Electrochim. Acta*, 2013, **89**, 479–487.